Fused Selenophene-thieno[3,2-b]thiophene-selenophene (ST)-based Narrow Bandgap Electron Acceptor for Efficient Organic Solar Cells with Small Voltage Loss

Journal:	*ChemComm*
Manuscript ID	CC-COM-05-2019-003585.R1
Article Type:	Communication

Journal Name

COMMUNICATION

Fused Selenophene-thieno[3,2-b]thiophene-selenophene (ST)-based Narrow Bandgap Electron Acceptor for Efficient Organic Solar Cells with Small Voltage Loss

Received 00th January 20xx,
Accepted 00th January 20xx

DOI: 10.1039/x0xx00000x

www.rsc.org/

Xunfan Liao*[a†], Xueliang Shi[b†], Ming Zhang[e], Ke Gao[c], Lijian Zuo[c], Feng Liu*[e], Yiwang Chen*[a], and Alex K-Y. Jen*[c,d]

A novel near-infrared absorbing fused-ring electron acceptor STIC was developed for organic solar cells. STIC exhibits a narrow bandgap with absorption edge reaching 940 nm, which ascribe to the strong electron-rich selenophene-thieno[3,2-b]thiophene-selenophene (ST) unit and strong intramolecular charge transfer of STIC. Besides, the rigid ST core provides low reorganization energy to enable a low open circuit voltage (Voc) loss in STIC based devices. The incorporation of Se atoms in STIC changed the intermolecular interaction with polymer PBDB-T and formed two relatively pure phases, which facilitates charge transport. The PBDB-T:STIC blend based device exhibits a power conversion efficiency (PCE) of 9.68% with a high short-circuit current density (Jsc) of 19.96 mA cm^{-2} and a low Voc loss of 0.55 eV.

Non-fullerene acceptors (NFAs) based organic solar cells (OSCs) have made significant advances recently due to their broad absorption in visible and near-infrared (NIR), easily adjustable energy levels, and tunable crystallinity in active layer morphology.[1-8] Currently, the most successful type of NFAs is the Acceptor-Donor-Acceptor (A-D-A) type fused-ring electron acceptors (FREAs) which is represented by the star molecule, ITIC, and its derivatives.[2, 9-13] There are several distinct advantages in FREAs compared with other types of acceptors. First, the A-D-A skeleton in FREA molecular framework can induce strong intramolecular charge transfer (ICT) through effective π-electron delocalization, thus reducing their bandgaps. Second, the FREAs have good molecular coplanarity and strong intermolecular interactions, which can decrease molecular rotational disorder and reorganization energy, and thus will contribute to high charge mobilities and low open circuit voltage (Voc) loss in they based OSCs. In addition, the solubility and film-forming property of FREAs could be controlled by using different side chains. Consequently, these characteristics enable FREAs based solar cells to achieve high power conversion efficiency (PCE).[9-18] A large number of highly efficient FREAs have been reported and the PCE of the state-of-the-art FREAs based device has already reached over 15%,[17-18] which shows great potential for commercial applications.

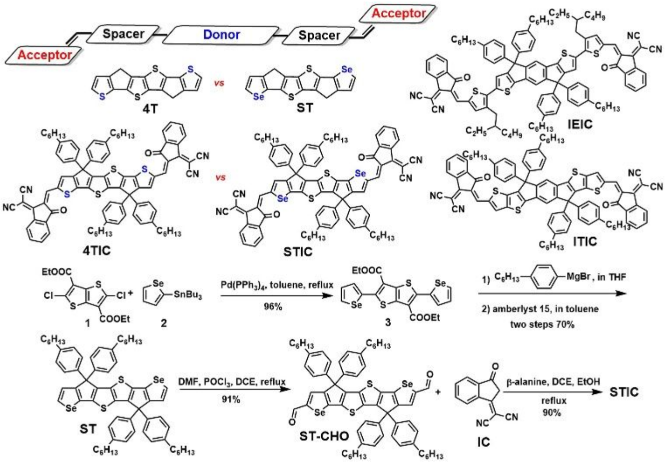

Scheme 1 Molecular design, chemical structures of NFAs and synthetic route to STIC.

One of the most straightforward ways to increase the efficiency of OSCs is to maximize the coverage of solar spectrum to efficiently harvest photons for high photocurrents. Thus, it is highly desirable to design low bandgap NFAs with broadened absorption to NIR (>800 nm) to sufficiently utilize the solar spectrum. The most simple and effective strategy to design narrow bandgap acceptors is to either enhance the central core's electron-donating ability to elevate the highest occupied molecular orbital (HOMO) energy level, or to enhance the accepting ability of terminal unit to decrease the lowest unoccupied molecular orbital (LUMO) energy level. This will result in improved ICT and reduced bandgap. However, it is noteworthy that the development of low bandgap NFAs is still lagging behind that of

---

[a] *State Key Laboratory for Modification of Chemical Fibers and Polymer Materials & College of Materials Science and Engineering, Donghua University, Shanghai 201620, China. E-mail: xfliao616@dhu.edu.cn; ywchen@dhu.edu.cn*
[b] *Shanghai Key Laboratory of Green Chemistry and Chemical Processes, School of Chemistry and Molecular Engineering, East China Normal University, Shanghai 200062, PR China*
[c] *Department of Materials Science and Engineering, University of Washington, Seattle, WA, 98195-2120, USA. E-mail: ajen@uw.edu*
[d] *Department of Chemistry, City University of Hong Kong, Kowloon 999077, Hong Kong*
[e] *School of Chemistry and Chemical Engineering, Shanghai Jiao Tong University, Shanghai 200240, China. fengliu82@sjtu.edu.cn*
† *These authors contributed equally to this work.*
Electronic Supplementary Information (ESI) available: Synthesis methodology and details of characterization. See DOI: 10.1039/x0xx00000x.

medium bandgap (>1.5 eV) acceptors. Thus, it is highly desirable to develop highly efficient narrow bandgap FREAs for OSCs.

Recently, a thiophene-thieno[3,2-b]thiophene-thiophene (4T) based low bandgap 4TIC, was successfully developed by Jen *et al.*,[19] and the results from a comprehensive study disclosed that the low resonance stabilization energy of central core is very effective in enhancing the ICT effect and thus shifting the absorption edge of 4TIC towards NIR. Based on this encouraging result, herein, we focus on another interesting donor unit, selenophene-thieno[3,2-b]thiophene-selenophene (ST), by replacing the outmost thiophene in 4T with selenophene, resulting in another narrow bandgap NFA, STIC, as shown in **Scheme 1**. It is expected that the change from sulfur atom in 4T to selenium atom in ST will endow STIC with several distinct properties, such as the relatively looser electron cloud delocalization of selenium atom will reduce orbital overlap with the adjacent π-system, resulting in decreased aromaticity/resonance energy of selenophene compared to that of thiophene. This will favor the quinoid resonance character of STIC at ground state to enhance the ICT and reduce its bandgap. Besides, the more polarizable selenium atom in STIC is also expected to enhance the intermolecular interactions to result in higher charge carrier mobility and improved solar cell performance.

As expected, the STIC exhibits a broadened optical absorption spectrum from 600 to 900 nm with the onset at ~940 nm, which red-shifts ~50 nm compared to that of 4TIC. The crystallographic analysis revealed that STIC has the similar molecular geometry and packing motif of 4TIC. The terminal groups in STIC form an even closer intermolecular π−π stacking with ~ 3.409 Å compared to that of 4TIC (3.536 Å), which will facilitate charge transport. As a result, STIC shows higher electron mobility (1.2×10^{-4} cm^2 V^{-1} s^{-1}) than that of 4TIC (9.07×10^{-5} cm^2 V^{-1} s^{-1}). When blended with the polymer donor PBDB-T, the PBDB-T:STIC based device show a PCE of 9.68% with a high short-circuit current density (Jsc) of 19.96 mA cm^{-2}, and a small Voc loss of 0.55 eV, which is comparable with those of 4TIC (PCE=10.2%, Jsc=19.13 mA cm^{-2}, Voc loss= 0.58 eV).

The synthesis of ST core and STIC follows the similar protocol for 4TIC,[19] and is shown in **Scheme 1**. Diester **3** was obtained in high yield by coupling the compound **1** and **2** using $Pd(PPh_3)_4$ as catalyst. Then diester **3** was reacted with nucleophilic (4-hexylphenyl)magnesium bromide in 1:2 molar ratio, followed by the Friedel−Crafts intramolecular cyclization induced by amberlyst 15 to afford the central core ST. Subsequently, the di-carbaldehyde monomer ST-CHO was prepared by the Vilsmeier-Haack reaction of ST with $POCl_3$ in N,N-Dimethylformamide (DMF). Finally, the target STIC was synthesized in 90% yield by the Knoevenagel condensation between ST-CHO and excess 1,1-dicyanomethylene-3-indanone (IC) in the presence of β-alanine. The detailed synthetic procedures for target acceptor were provided in the ESI and all the intermediates and target acceptor were characterized by conventional NMR and mass spectroscopy (**Fig. S1-12** in the ESI).

The UV-vis absorption spectra of 4TIC and STIC in dichloromethane (DCM) solution and in thin film are recorded as shown in **Fig. 1a**, and the related data are summarized in **Table S2** (ESI). In solution, STIC exhibits a strong absorption band at 600-850 nm with the maximum absorption at 768 nm, which red-shifts ~30 nm compared to that of 4TIC. In thin film, the absorption of STIC further red-shifts to NIR region with the absorption edge at ~940 nm, while the absorption edge for 4TIC is 886 nm. The energy levels of STIC and 4TIC were studied by cyclic voltammetry (CV) measurements in DCM solution, as shown in **Fig. 1b**. The HOMO/LUMO energy levels of STIC and 4TIC were calculated from the onset oxidation and reduction potentials with values of -5.20/-3.91 and -5.28/-3.87 eV, respectively. STIC shows a higher HOMO energy level than that of 4TIC, which is owing to the stronger electron-donating ability of ST unit. And the ST central core can induce stronger ICT effect with terminal IC groups, affording a lower LUMO energy level in STIC. Consequently, the STIC has a much narrower electronic bandgap (HOMO-LUMO gap) than that of 4TIC (**Table S2** in the ESI).

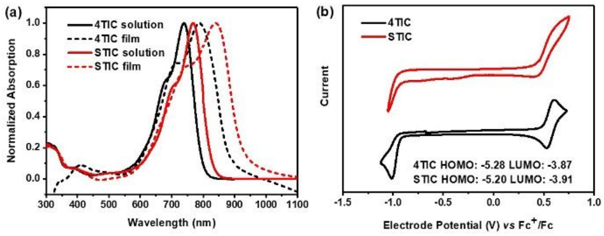

Fig. 1 (a) UV−vis−NIR spectra of 4TIC and STIC in the DCM solution and thin film. (b) Cyclic voltammograms of 4TIC and STIC.

To further understand the difference of energy levels between 4TIC and STIC, density functional theory (DFT) calculations with B3LYP/6-31G(d,p) level were also used to calculate their (4T's, ST's, 4TIC's and STIC's) electron density distributions, and HOMO and LUMO energies. The results from DFT calculations elucidate that there is no significant effect on the electron density distributions of the HOMO and LUMO after the exchange of chalcogen, as shown in **Fig. S13**. However, it has significant impact on their HOMO and LUMO energy levels. Specifically, ST has a 0.024 eV increase in HOMO level and a 0.038 eV decrease in LUMO level compared to 4T. Similarly, the calculated STIC HOMO level is 0.045 eV higher and LUMO level is 0.011 eV lower than those of 4TIC, which cause a narrower bandgap.

Single crystals of STIC suitable for single-crystal X-ray diffraction analysis were obtained for investigating the geometry and packing behaviour of the molecule. The Oak Ridge Thermal Ellipsoid Plot (ORTEP) drawings and three-dimensional (3D) packing structures of STIC are presented in **Fig. 2**, and those of 4TIC are also shown for comparison. The π-frameworks of two molecules are almost planar due to the rigidity of fused ST and 4T (**Fig. 2**, side-view). The high planarity of STIC and 4TIC is also benefitted from the unique interaction between terminal IC group and central ST and 4T unit. Particularly, the terminal IC and central ST and 4T can interlock via the intimate [Se···O] interactions in STIC and [S···O] interactions in 4TIC (**Fig. 2**, top-view), resulting in a sole pattern of molecular geometry and the enhanced molecular planarity although the terminal IC can rotate freely because of the single bond connection. No obvious intermolecular interactions could be found in the ST and 4T central cores due to the four bulky hexylphenyl groups oriented almost perpendicularly to the backbone of ST and 4T unit. Instead, the terminal IC groups can form a close intermolecular π−π stacking with a distance of ~3.409 Å and 3.536 Å for STIC and 4TIC, respectively (**Fig. 2**, 3D packing). The shorter intermolecular π−π stacking distance in STIC may not only enhance charge carrier mobility but also reduce non-radiative bimolecular recombination to result in smaller Voc loss.

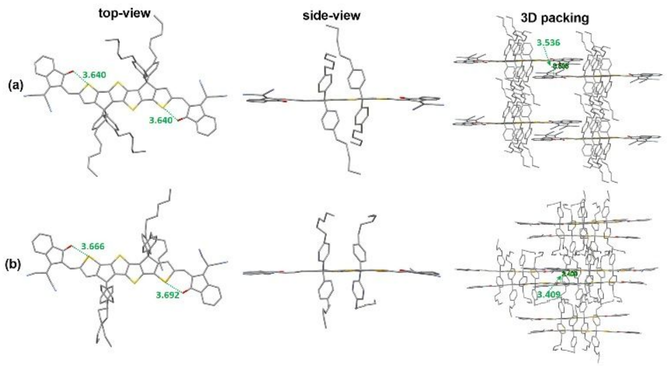

Fig. 2 X-ray crystallographic structure of 4TIC (a) and (b) STIC. Hydrogen atoms are omitted for the sake of clarity.

To evaluate the photovoltaic performance of STIC and 4TIC derived solar cells, bulk-heterojunction (BHJ) devices with the configuration of ITO/PEDOT:PSS/PBDB-T:STIC or 4TIC/C_{60}-bissalt/Ag were fabricated. As shown in **Fig. 3a** and **Table 1**, the PBDB-T:STIC based as-cast devices gave a moderate PCE of 7.94%. After the addition of 0.5% 1,8-diiodooctane (DIO), the PCE significantly increased to 9.68% with a Voc of 0.77 V, an impressive Jsc of 19.96 mA/cm^2, and a fill factor (FF) of 0.63. In comparison, STIC has a slightly higher Jsc than 4TIC (19.13 mA/cm^2) due to its red-shifted absorption. Moreover, STIC exhibited a lower Voc loss (0.55 eV) than that of 4TIC (0.58 eV). The smaller Voc loss might result from the lower reorganization energy of STIC. However, the Voc and FF of STIC are lower than those reported for 4TIC owing to its decreased LUMO energy level and different structural order and morphology of the BHJ blended films (vide infra).

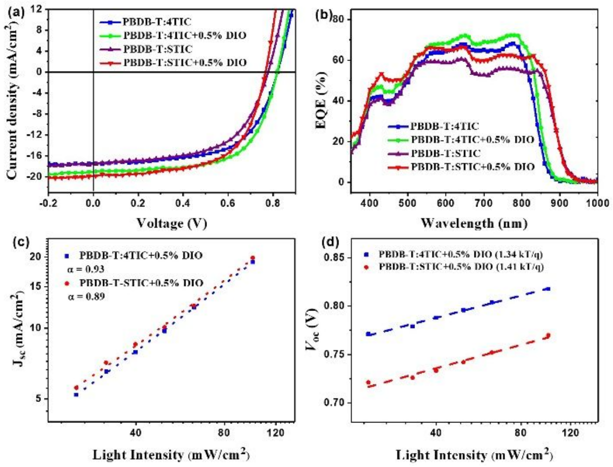

Fig. 3 (a) J–V and EQE (b) curves of the OSCs. Light intensity dependence of Jsc (c) and Voc (d) of the optimized device.

The morphology of the BHJ film could be optimized by adding DIO to facilitate charge transport. To prove this point, the electron mobilities of the blended films were measured by using the space-charge-limited-current (SCLC) method (shown in **Fig. S14** and **Table S3** in the ESI).[20-21] The as-cast device exhibited an electron mobility as high as 4.19×10^{-5} cm^2 V^{-1} s^{-1} and 5.21×10^{-5} cm^2 V−1 s^{-1} for PBDB-T:4TIC and PBDB-T:STIC, respectively. After the 0.5% DIO treatment, the electron mobility of PBDB-T:STIC based device could be significantly increased to 1.2×10^{-4} cm^2 V^{-1} s^{-1}, which agrees well with closer packing indicated in the single crystals data. Therefore, the higher Jsc and FF values should be derived from the improved charge mobility. The increased Jsc could also be confirmed through the measurement of their external quantum efficiencies (EQEs) spectra, as shown in **Fig. 3b**. The Jsc values calculated from the EQE curves are 17.03, 18.65, 17.08 and 19.06 mA cm^{-2} for PBDB-T:4TIC, PBDB-T:4TIC with DIO, PBDB-T:STIC and PBDB-T:STIC with DIO devices, respectively, which are within reasonable match with the Jsc values measured from the corresponding J–V curves.

Table 1. Photovoltaic parameter of OSCs based on PBDB-T:Acceptor

Active layer	Voc (V)	Jsc (mA/cm^2)	FF	PCE (%)^b
PBDB-T:4TIC	0.82	17.38	0.62	8.84
PBDB-T:4TIC^a	0.82	19.13	0.65	10.2
PBDB-T:STIC	0.78	17.56	0.58	7.94
PBDB-T:STIC^a	0.77	19.96	0.63	9.68

^{a}Treatment with 0.5% DIO; ^{b}Average values obtained from ten devices are shown in parentheses.

To investigate the mechanism of carrier recombination in the STIC and 4TIC devices, the light intensity–dependent measurements of Jsc and Voc were conducted. In general, the relationship between Jsc and incident light intensity (I) follows a power-law formula of Jsc $\propto I^{\alpha}$, where the slope of the curve (α) approaching 1 implies that the bimolecular recombination is negligible.[22-24] As shown in **Fig. 3c**, the α values of the STIC and 4TIC-based devices are 0.89 and 0.93, respectively, indicating less charge recombination loss during charge extraction in the 4TIC-based devices, which further supports its higher FF compared with PBDB-T:STIC.[31-32] In addition, the dependence of Voc on the light intensity for PBDB-T:4TIC based device was recorded with a slope of 1.34 kT/q, compared to that of 1.41 kT/q for PBDB-T:STIC based device (**Fig. 3d**), also indicating that less trap-assisted recombination in PBDB-T:4TIC based devices.

The morphology of BHJ films play a vital role in determining the OSCs performance.[25-26] Thus, a systematic morphological study including structural order and phase segregation was performed. **Fig. S15a** (ESI) showed the 2D grazing incidence X-ray diffraction (GIXD) pattern of STIC pure film and the corresponding 1D line cuts was shown in **Fig S15b** (ESI). Relative results of 4TIC was previous reported,[19] which showed a mainly face-on orientation, with (100) diffraction at 0.46 Å^{-1} in the in-plane direction, corresponding to a distance of 1.36 nm, and (010) peak at 1.84 Å^{-1}, corresponding to a distance of 0.34 nm. STIC showed a preferred edge-on orientation, with a distinct (100) diffraction at 0.40 Å^{-1} in the out-of-plane direction and (010) peak at 1.78 Å^{-1} in the in-plane direction. Although the replacement of thiophene with selenophene in STIC dramatically changed the molecular packing of the solid state, it still maintained the crystalline feature due to its strong intermolecular interaction and self-assembly capability.

In BHJ blends, PBDB-T diffraction dominated the 2D pattern (shown in **Fig. 4a**). Peak at 0.30 Å^{-1} in the in-plane direction and 1.71 Å^{-1} in the out-of-plane direction was (100) and (010) diffraction from PBDB-T, respectively, similar with those previously reported.[27] The fitting results of (010) diffraction was showed in **Table S4** (ESI). The addition of DIO promoted a better structure, with a closer packing, induced crystal size and crystallinity, which could be proven by the changed d-spacing, crystal coherence length and peak area for both blends. This is the reason why the addition of DIO could significantly improve device performance, especially Jsc and FF. STIC blends were shown to be more crystalline. In the 4TIC blends, polymer showed closer packing distance, which facilitated electron hopping, resulting a high FF. The crystallization of acceptors was supressed in blends, therefore no distinct peaks from acceptor could be observed.

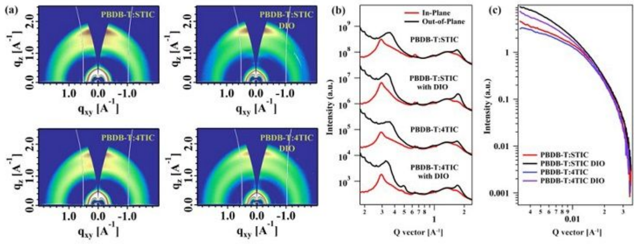

Fig. 4 (a) Grazing incidence X-ray diffraction patterns of BHJ blends. (b) In-plane (red lines) and out-of plane (black lines) line-cut profiles of GIXD results. (c) Resonant soft X-ray scattering of BHJ blends.

Resonant soft X-ray scattering (RSoXS) at 285 eV was used to study the length scale of phase separation of the blended films, and the corresponding results were shown in **Figure 4c**. A broad and elevated hump from 0.02 Å^{-1} to 0.008 Å^{-1} could be observed, indicating a quite broad distribution of phase separation length scale. To achieve the average domain size, curves of Iq2 versus q were plotted in **Fig. S15c** (ESI). While PBDB-T:4TIC showed a center-to-center distance of 48.5 nm and 57.2 nm for the as cast and DIO-modified blends, PBDB-T:STIC displayed a center-to-center distance of 48.3 nm and 58.2 nm, respectively. Increased domain size not only benefitted carrier transport but also didn't hamper exciton splitting within this scale, therefore contributed to the improved Jsc and FF. The STIC blends exhibited stronger scattering intensity due to the incorporation of Se atoms changed the intermolecular interaction with polymers, causing worsen miscibility and the formation of two relatively pure phases (polymer-rich and small-molecule-rich), with more contrast. Purer phase region was conducive for carrier transport, thus STIC showed higher electron mobility.

In summary, a novel electron-rich central building block ST and a derivative NIR-absorbing fused-ring electron acceptor STIC have been successfully developed for OSCs. The structure of STIC is similar to that previously reported 4TIC, by just replacing the outmost thiophene in 4T with selenophene. The results from the study of single crystals reveal that STIC has a smaller intermolecular π–π stacking distance than 4TIC, resulting in increased electron mobility. In addition, STIC possesses stronger NIR absorption with a narrower bandgap of 1.32 eV than that of 4TIC (1.40 eV), which is beneficial for achieving high Jsc in OSCs. As result, the PBDB-T:STIC based device exhibits a higher Jsc of 19.96 mA cm^{-2} along with a smaller Voc loss (0.55 eV). Our results demonstrate that ST is an effective building block for constructing NIR-absorbing NFAs for efficient OSCs.

The authors acknowledge financial support from the "the Fundamental Research Funds for the Central Universities" (2232019D3-04), Shanghai Sailing Program (19YF1401000), the Initial Research Funds for Young Teachers of Donghua University, the Office of Naval Research (N00014-17-1-2201), the National Science Fund for Distinguished Young Scholars (51425304), and the Young 1000 Talents Global Recruitment Program of China. X-ray data was acquired at beamline 7.3.3 and 11.0.1.2 at Lawrence Berkeley National Laboratory, which is supported by the DOE, Office of Science, and Office of Basic Energy Sciences.

Notes and references

1 Y. Zhang, L. Shi, Y, Chen, *Acta Polym. Sin*., 2019, **50**, 13-26.
2 Y. Lin, J. Wang, Z. G. Zhang, H. Bai, Y. F. Li, D. B. Zhu, X. W. Zhan, *Adv. Mater*., 2015, **27**, 1170-1174.
3 C. Yan, S. Barlow, Z. Wang, H. Yan, A. K.-Y. Jen, S. R. Marder, X. Zhan. *Nat. Rev. Mater*., 2018, **3**, 18003.
4 S. Chen, H. Cho, J. Lee, Y. Yang, Z. Zhang, Y. Li, C. Yang, *Adv. Energy Mater*., 2017, 1701125.
5 M. Jeong, S. Chen, S. Lee, Z. Wang, Y. Yang, Z. Zhang, C. Zhang, M. Xiao, Y. Li, C. Yang, *Adv. Energy Mater*., 2017, 1702166.
6 S. P. Mishra, A. E. Javier, R. Zhang, J. Liu, J. A. Belot, I. Osaka and R. D. McCullough, *J. Mater. Chem.*, 2011, **21**, 1551-1561.
7 J. Kim, S. Park, S. Lee, H. Ahn, S. Joe, B. Kim, H. Son, *Adv. Energy Mater*., 2018, **8**, 1870132.
8 X. Liao, J. Wang, S. Chen, L. Chen, Y. Chen, *Chin. J. Polym. Sci*., 2016, **34**, 491-504.
9 W. Zhao, S. Li, S. Zhang, X. Liu, J. Hou, *Adv. Mater*., 2017, **29**, 1604059.
10 Y. Yang, Z. Zhang, H. Bin, S. Chen, L. Xue, C. Yang, Y. Li, *J. Am. Chem. Soc*., 2016, **138**, 15011-15018.
11 H. Yao, Y. Cui, R. Yu, B. Gao, H. Zhang, J. Hou, *Angew. Chem., Int. Ed.*, 2017, **56**, 3045-3049.
12 C. Huang, X. Liao, K. Gao, L. Zuo, F. Lin, X. Shi, C.-Z. Li, F. Liu, Y. Chen, H. Chen, A. K.-Y. Jen, *Chem. Mater*., 2018, **30**, 5429-5434.
13 R. Singh, J. Lee, M. Kim, P. E. Keivanidis and K. Cho, *J. Mater. Chem. A*, 2016, **5**, 210–220.
14 Z. Yao, X. Liao, K. Gao, F. Lin, X. Xu, X. Shi, L. Zuo, F. Liu, Y. Chen, A. K. Y. Jen, *J. Am. Chem. Soc*., 2018, **140**, 2054-2057.
15 A. Mishra, M. Keshtov, A. Looser, R. Singhal, M. Stolte F. Würthner, P. Bäuerle, G. Sharma, *J. Mater. Chem. A*, 2017, **5**, 14887-14897.
16 Z. Xiao, X. Jia, L. Ding, *Sci. Bull*., 2017, **62**, 1562-1564.
17 J. Yuan, Y. Zhang, L. Zhou, G. Zhang, H. Yip, T. Lau, X. Lu, C. Zhu, H. Peng, P. Johnson, et al. Joule, 2019, **3**, 1-12.
18 B. Fan, D. Zhang, M. Li, W. Zhong, Z. Zeng, L. Ying, F. Huang, Y. Cao, *Sci. China Chem*., 2019, DOI: 10.1007/s11426-019-9457-5.
19 X. Shi, L. Zuo, S. Jo, K. Gao, F. Lin, F. Liu, A. K.-Y. Jen, *Chem. Mater*. 2017, **29**, 8369-8376.
20 J. Yuan, L. Qiu, Z. Zhang, Y. Li, Y. Chen, Y. Zou, *Nano Energy*, 2016, **30**, 312-320.
21 M. Li, K. Gao, X. Wan, Q. Zhang, B. Kan, R. Xia, F. Liu, X. Yang, H. Feng, W. Ni, Y. Wang, J. Peng, H. Zhang, Z. Liang, H. Yip, X. Peng, Y. Cao, Y. Chen, *Nat. Photonics*, 2017, **11**, 85.
22 X. Chen, B. Liu, Y. Zou, L. Xiao, X. Guo, Y. He, Y. F. Li, *J. Mater. Chem*., 2012, **22**, 17724-17731.
23 A. K. K. Kyaw, D. H. Wang, V. Gupta, W. L. Leong, L. Ke, G. C. Bazan, A. J. Heeger, *ACS Nano*, 2013, **7**, 4569-4577.
24 R. Ingo, P. Jürgen, D. Vladimir, L. Laurence, V. Dirk, C. H. Jan. *Adv. Funct. Mater*., 2004, **14**, 38-44.
25 L. Ye, S. Li, X. Liu, S. Zhang, M. Ghasemi, Y. Xiong, J. Hou, H. Ade, *Joule*, 2019, **3**, 443-458.
26 X. Liao, L. Zhang, L. Chen, X. Hu, Q. Ai, W. Ma, Y. Chen, *Nano Energy,* 2017, **37**, 32-39.
27 W. Gao, T. Liu, C. Zhong, G. Zhang, Y. Zhang, R. Ming, L. Zhang, J. Xin, K. Wu, Y. Guo, et al. *ACS Energy Lett*. 2018, **3**, 1760-1768.

Table of Content:

A novel NIR-absorbing fused-ring electron acceptor STIC was successfully developed for organic solar cells and achieved a PCE of 9.68%.